International Journal of Technology

http://ijtech.eng.ui.ac.id

Research Article

Detection of Weld Defects in Steel Pipes Using a Coaxial Magnetic Induction Sensor: Numerical Simulation and Experimental Validation

Kurnia Nugraha[1,3,5], Winarto Winarto [2*], Didied Haryono[2,5], Imamul Muttakin[4,5], Amalia Sholehah[2,5], Agussutrisno[4,5], Riski Kurniawan[3], Nazwa Raudya Tuzahra[2]

[1]Department of Metallurgical and Material Engineering, Faculty of Engineering, Universitas Indonesia, Depok 16424, Indonesia

[2]Department of Metallurgical Engineering, Faculty of Engineering, Universitas Sultan Ageng Tirtayasa, Cilegon 42434, Indonesia

[3]Department of Mechanical Engineering, Faculty of Engineering, Universitas Sultan Ageng Tirtayasa, Cilegon, 42434, Indonesia

[4]Department of Electrical Engineering, Faculty of Engineering, Universitas Sultan Ageng Tirtayasa, Cilegon, 42434, Indonesia

[5]Laboratorium Advanced Materials and Tomography, Engineering Faculty, Universitas Sultan Ageng Tirtayasa, Cilegon 42434, Indonesia

[*]Corresponding author: winarto.msc@ui.ac.id; Tel.: +628128122407; Fax: +62217872350

Abstract: Weld defects in high-pressure piping systems are critical initiation points for leakage, rupture, or explosion, leading to severe safety hazards and economic losses. Therefore, reliable and early detection methods are essential for ensuring the integrity of industrial pipelines. Radiographic testing (RT) is widely used because of its ability to produce detailed internal images. However, RT relies on hazardous ionizing radiation, requires certified operators, and incurs high operational costs. These limitations drive the need for safer and more efficient alternatives. Magnetic induction tomography (MIT) is a radiation-free, non-contact, and operationally simple method; however, its insufficient spatial resolution and sensitivity, especially for sub-millimeter flaws, limit its industrial deployment. To address these challenges, a coaxial magnetic induction (CMI) sensor specifically engineered for weld-defect detection is developed and evaluated in this study. The sensor employs a concentric transmitter-receiver configuration that enhances electromagnetic coupling, improves spatial resolution, and suppresses external noise compared with conventional sensing architectures. In this report, we employ controlled laboratory experiments, impedance-based signal analysis, and principal component analysis (PCA) to systematically investigate the sensor's response to defects. Experiments conducted on steel plates and welded pipes containing 0.5-2.0 artificial defect revealed a clear proportional relationship between the defect size and the induced-voltage variation. Statistical validation confirmed excellent measurement repeatability (CV $< 2.5\%$) and significant separation between the defective and non-defective groups ($p < 0.01$). These results confirm that the proposed CMI sensor addresses the critical limitations of conventional MIT systems and offers a safer, radiation-free, and cost-efficient approach to weld-defect detection, thereby meeting the industrial safety requirements highlighted at the outset.

Keywords: Coaxial sensor; Magnetic induction tomography; Non-destructive testing; Steel pipes; Weld defects

1. Introduction

Welded joints are critical structural components in high-pressure piping systems widely used in the petrochemical, oil, and gas industries (Guan et al., 2025). Their ability to main-

https://doi.org/10.14716/ijtech.v17i1.8211
Received July 2025; Revised November 2025; Accepted November 2025

tain mechanical continuity and retain internal pressure is highly dependent on the weld quality, as defects such as voids, inclusions, and incomplete fusion can generate localized stress concentrations that may lead to leakage, rupture, or catastrophic failure (Pipeline and Hazardous Materials Safety Administration, 2022; Kou, 2003). These risks carry substantial safety and economic implications, making early and accurate weld-defect detection essential for effective management of industrial integrity.

The increasing global demand for steel pipelines, as reported by Grand View Research (Grand View Research, 2024), further highlights the importance of robust inspection technologies capable of ensuring operational reliability and preventing unplanned shutdowns. Alongside inspection, pipeline failure prediction and determining optimal replacement intervals have become increasingly critical. Recent data-driven studies have demonstrated that machine learning approaches, such as random forest and binary logistic regression, have a strong capability for assessing failure risk and supporting maintenance scheduling (Noorsaman et al., 2023).

Radiographic testing (RT) is currently the most widely used and recognized nondestructive testing (NDT) method for the early detection of weld defects and for evaluating the integrity of welded joints in industrial piping systems. Its popularity is largely attributed to its ability to produce high-resolution internal images that enable accurate identification and characterization of subsurface flaws (Gupta et al., 2022; Shaloo et al., 2022; Deepak et al., 2021). However, RT has several limitations: it involves hazardous ionizing radiation, which raises significant health and safety concerns. It requires specialized equipment and trained personnel, which incurs high operational costs and regulatory burdens. These limitations motivate the search for alternative NDT approaches with comparable detection performance while offering improved safety, lower cost, and greater operational simplicity.

Magnetic induction tomography (MIT) has emerged as a promising alternative NDT technique based on electromagnetic induction that enables noncontact, radiation-free imaging of conductive materials. At MIT, an alternating current is applied to an excitation coil to generate a time-varying primary magnetic field that induces eddy currents within the conductive medium. These eddy currents generate a counteracting secondary magnetic field, which is detected by the receiving coil as variations in the complex impedance or mutual inductance. The conductivity distribution can be reconstructed from these variations. (Schledewitz et al., 2024; Schledewitz et al., 2023; Piscitelli et al., 2023; Tan et al., 2021; Dingley and Soleimani, 2021; Klein et al., 2020; Ma and Soleimani, 2017; Mansor et al., 2015; Ma, 2014; Wei and Soleimani, 2012 Griffiths, 2001). Internal defects disturb the eddy-current distribution and the resulting secondary magnetic field, enabling the reconstruction of the spatial conductivity maps through appropriate inversion algorithms (Schledewitz et al., 2023; Yang et al., 2021; Tan et al., 2021; Klein et al., 2020; Chen et al., 2020, Chen et al., 2019; Feldkamp, 2017).

MIT has undergone substantial development and has been successfully applied across a wide range of fields, including industrial process monitoring (Muttakin and Soleimani, 2020; Muttakin et al., 2020; Guilizzoni et al., 2019; Ma et al., 2017), bioimpedance imaging (Cao et al., 2024; Zhu et al., 2023; Hofmann et al., 2022; Klein et al., 2020), materials characterization, and nondestructive evaluation (Schledewitz et al., 2023; Piscitelli et al., 2023; Klein et al., 2020; Al Huda et al., 2020; Ma, 2014; Wei et al., 2012). These achievements demonstrate the versatility of MIT as an electromagnetic imaging technique for both scientific and industrial applications. Despite these advancements, the application of MIT to welded steel structures remains limited. The inherently shallow skin depth in highly conductive metals, the high electrical conductivity of steel, the low signal-to-noise ratio (SNR), and the geometric complexity of welded joints collectively constrain the ability of MIT to achieve adequate spatial resolution and flaw sensitivity (Klein et al., 2020; Ma and Soleimani, 2017). These unresolved challenges highlight a clear technological gap and underscore the need for performance enhancements tailored to high-conductivity metallic systems.

Efforts to improve the performance of MIT generally follow two principal directions. The first focuses on sensor and coil architectures advancements to strengthen electromagnetic cou-

pling, enhance defect sensitivity, and suppress noise. The second approach improved signal modeling and inverse reconstruction approaches to enhance feature extraction and stabilize the inverse problem's inherently ill-posed nature. Representative developments include three-dimensional MIT for volumetric imaging (Klein et al., 2020; Wei et al., 2012), compact coreless coils with ultra-high magnetic sensitivity (Ratajczak and Wondrak, 2020), Helmholtz configurations (Zhu et al., 2023), biplane enhancements (Cao et al., 2024), and gradiometer arrays (Xiao et al., 2019). However, the rigorous validation of these methods on welded steel specimens remains scarce. High conductivity, reduced skin depth, and complex weld geometries intensify the trade-off between spatial resolution and SNR.

Motivated by this gap, the present study introduces the coaxial magnetic induction (CMI) sensor, derived from patent number IDS000008689 owned by Universitas Sultan Ageng Tirtayasa (Haryono et al., 2024), and specifically designed to enhance the sensitivity for detecting voids and inclusions in steel pipe welds. The concentric transmitter–receiver architecture strengthens the magnetic-field coupling and suppresses external electromagnetic interference, thereby lowering the submillimeter-scale detection threshold. The CMI sensor offers a safer, radiation-free, and more operationally practical alternative to RT through these improvements. The scope of this research includes multiphysics-based sensor optimization, prototype fabrication, experimental validation of welded specimens, and signal characterization using principal component analysis (PCA). This study focuses on the signal-based performance evaluation, while full conductivity image reconstruction is identified as future work.

2. Methods

This study involved the design, multiphysics modeling, fabrication, and experimental validation of the CMI sensor for detecting voids and inclusions in steel-pipe welds. The methodological framework consisted of (i) numerical optimization of sensor architecture and operating parameters, (ii) prototype development, and (iii) controlled laboratory measurements on steel plates and industrial steel pipes containing artificial defects. Subsequent analyses included impedance or induced-voltage extraction, spectral feature clustering using principal component analysis (PCA) over 8 Hz–32 kHz, and statistical validation of the optimal operating band (40–100 kHz), which exhibited low measurement variability (CV $< 2.5\%$) and significant class separation (t-tests, Hotelling's T^2; $p < 0.01$).

2.1 Coaxial Sensor

The coaxial magnetic induction (CMI) sensor was configured based on a previously filed patent design (IDS000008689, Universitas Sultan Ageng Tirtayasa) (Haryono et al., 2024). The transmitter (Tx) and receiver (Rx) coils are aligned along a common axis, enabling the magnetic flux concentration within the region of interest (ROI) and enhancing the sensitivity and spatial resolution while reducing susceptibility to external electromagnetic interference.

The sensor comprises a small-diameter Tx coil and a high-turn Rx coil separated by an adjustable insulating spacer to define the Tx–Rx distance. The assembly is housed in a rectangular enclosure equipped with an internal conductive liner to improve electromagnetic shielding.

The sensor operates based on the principle of electromagnetic induction (Figure 1), wherein the transmitting coil (Tx), driven by an alternating current, generates a time-varying primary magnetic field that induces the eddy currents within the conductive specimen. Subsequently, the receiving coil (Rx) detects variations in the induced voltage resulting from the interaction of these fields. Any disturbance in the eddy current distribution, such as the presence of voids or inclusions within the specimen, alters the signal characteristics measured by the Rx, thereby enabling the identification of internal defects in the material.

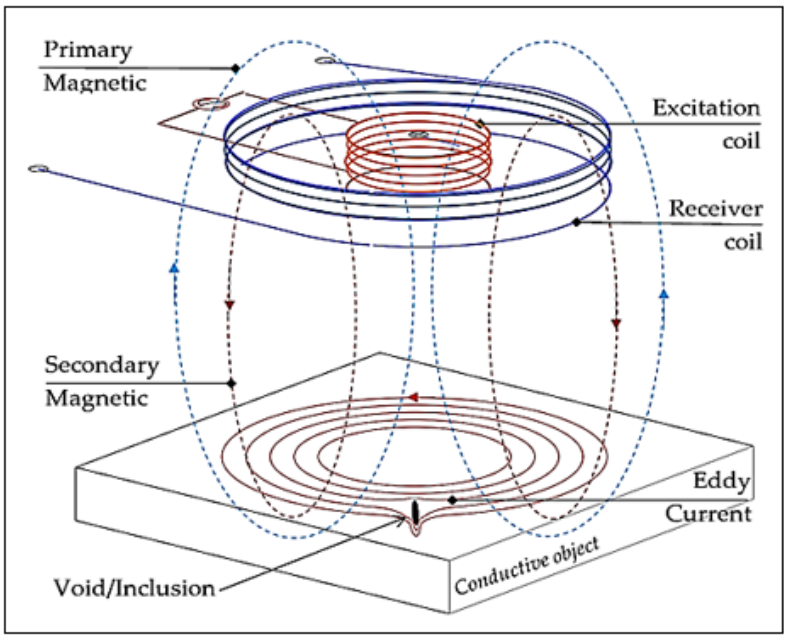

Figure 1 Fundamental principles of the CMI sensor

2.2 Numerical Simulation

The CMI sensor was designed and optimized using multiphysics simulations following established electromagnetic modeling practices (Nugraha et al., 2026; Puji et al., 2024; Ishak et al., 2021). The optimal coil geometry and operating conditions determined from the parametric analysis were selected for the fabrication of the prototype and subsequent experiments.

2.2.1 Sensors Parameters

The simulation model incorporates a coaxial transmitter-receiver (Tx–Rx) coil pair constructed from copper wire (Figure 2). The Tx coil consists of 115 turns with outer and inner diameters of 5 and 3 mm, respectively, whereas the Rx coil contains 1150 turns with diameters of 15 and 6 mm. Both coils are 10 mm, forming a compact coaxial structure suitable for localized inspection.

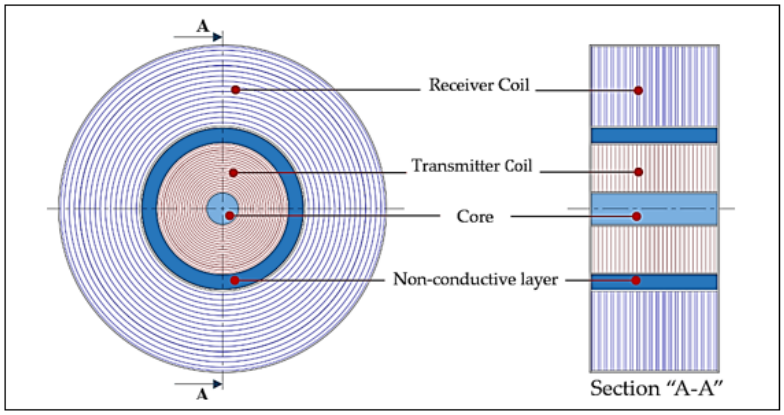

Figure 2 Coaxial magnetic induction (CMI) sensor model

2.2.2 Geometry and Defect Modeling

The simulation model represents a steel pipe with a length of 500 mm, outer diameter of 114.3 mm, inner diameter of 102.26 mm, and wall thickness of 6.02 mm. To evaluate the sensor's

capability in detecting subsurface size, dependent defects, cylindrical voids with diameters of 0.5, 1.0, 1.5, and 2.0 mm were embedded beneath the pipe surface to evaluate the defect-sizing capability. The geometric parameters of the modeled pipe were designed to match the industrial specimen used in the experimental validation.

2.2.3 Meshing

A free tetrahedral mesh with a fine resolution setting was used to discretize the computational domain. The mesh parameters were configured as follows: minimum element size of 2.4 mm, maximum element size of 33 mm, maximum growth rate of 1.4, curvature factor of 0.4, and narrow-region resolution of 0.7. The final mesh comprised 155,464 domain elements, 15,644 boundary elements, and 1,036 edge elements.

A mesh convergence analysis was conducted by uniformly refining the mesh by reducing both the minimum element size and the growth rate to verify the numerical accuracy. The resulting variations in the radial voltage response (VRx) and impedance magnitude ($|Z|$) at representative frequencies were less than 2%, confirming the numerical stability and sufficient resolution for electromagnetic modeling.

2.3 Experimental setup and measurements

The experimental system employed an MIT platform from C-TECH Labs Edwar Technology, comprising a magnetic-induction sensor interface, data-acquisition (DAQ) hardware, and a computer for signal processing and visualization (Nugraha et al., 2025).

2.3.1 Testing installation

During the experimental phase, a portable measurement device (Figure 3) was used to acquire the sensor responses. A magnetic-induction sensor, a compact DAQ module, and a computer for signal processing and real-time visualization are integrated into the device. This configuration allows for flexible on-site measurements while maintaining independent sensing, acquisition, and processing functions.

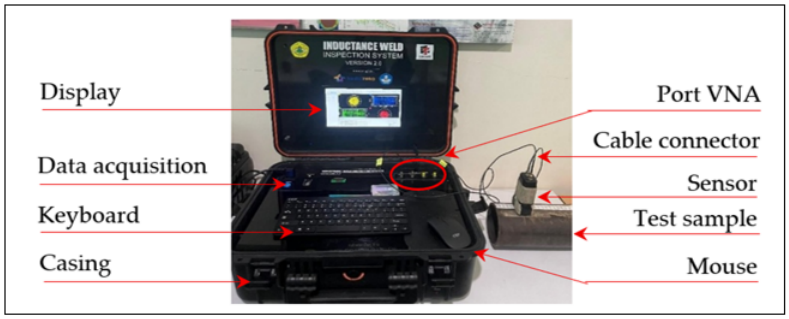

Figure 3 Portable testing device used in the experimental stage

2.4 Test Material

The experimental investigation involved two specimens, a steel plate containing predefined subsurface defects (50 × 50 × 10 mm) and an industrial-grade steel pipe (OD = 114.3 mm; ID = 102.26 mm; WT = 6.02 mm; L = 500 mm). The pipe was examined using ultrasonic testing (UT) before the magnetic-induction measurements to ensure accurate characterization of the internal geometry and potential anomalies. The UT data served as supplementary reference information during the analysis.

3. Results and Discussion

This section presents the numerical and experimental findings obtained from the MIT system. The results are divided into two main parts: (i) simulation analyses performed using multiphysics modeling to evaluate the electromagnetic response of the sensor, and (ii) experimental validation to confirm the system's capability in detecting weld defects under realistic conditions.

3.1 Simulation Results Using Multiphysics Software

3.1.1 Receiver coil voltage at a constant resistor

Figure 4a. Receiver-coil voltage VRx (mV) as a function of frequency (8 Hz–32 kHz) for Tx of 10–50 V with a 100 Ω series resistor. Below 80 Hz, VRx remained near the noise floor, indicating weak induction. From 8 Hz to 8 kHz, VRx rises sharply, marking the most sensitive band. Above 8 kHz, the slope tapers and the onset of saturation is evident at 10-20 V, reflecting reduced efficiency at higher frequencies, consistent with Faraday's law and high-frequency attenuation.

3.1.2 Receiver coil voltage at a constant transmitter voltage

Figure 4b. Receiver coil voltage VRx (mV) versus excitation frequency (8 Hz–32 kHz, log scale) for load resistances R_L = 50, 100, 500, 1000 Ω at a fixed transmitter drive of 10 V_rms. The VRx increases with frequency across all loads, with a steeper increase toward the upper band. At low frequencies, smaller R_L (50–100 Ω) yields higher VRx due to greater current in the predominantly resistive Rx branch; at higher frequencies, larger R_L (500–1000 Ω) provides a more favorable impedance division (inductive/capacitive reactance), improving the measurable voltage at Rx. These trends highlight the role of impedance matching in sensitivity and SNR.

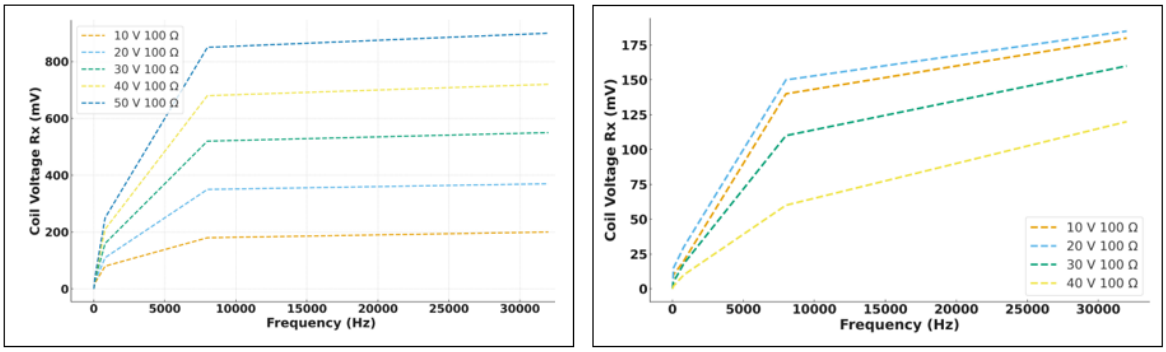

(a) (b)

Figure 4 Receiver coil voltage vs. frequency (a) constant resistance (b) constant transmitter voltage

3.1.3 Receiver Voltage of Non-Defective and Defective Specimens

Figure 5. Simulated receiver-coil voltage VRx (mV) for non-defective and defective specimens over 20–200 kHz. Both responses peak at ≈60 kHz, and the largest defect/non-defect separation lies within 40–100 kHz, indicating the best trade-off between penetration and sensitivity. In both cases, VRx declined at higher frequencies (>120 kHz), but the decline was steeper in the non-defective specimen. This simulated optimum coheres with the experimental operating band of 40–100 kHz, where measurements demonstrated high repeatability and significant class differences: the band benefits from a sufficient skin depth to interrogate near-weld volumes while boosting SNR through stronger eddy-current coupling; conversely, the reduced penetration lowers contrast, much above this range, and the weaker induction limits SNR. Ac-

cordingly, a higher VRx under defective conditions reflects the eddy-current distribution and secondary field perturbations, providing a robust defect identification signal-level indicator.

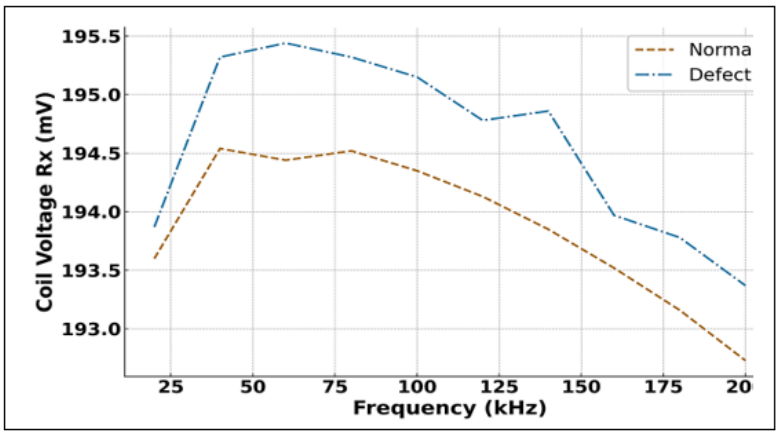

Figure 5 Receiver coil voltage on the nondefective and defective specimens

3.2 Experimental Results

Following the simulation study, experimental measurements were conducted on the defective and non-defective steel specimens using the developed CMI sensor. This section outlines the impedance and voltage response characteristics, supported by statistical and multivariate analyses, to evaluate the sensor's performance in differentiating the defect conditions. The results strongly agree with the simulation trends and highlight the effectiveness of the sensor in practical defect detection scenarios.

3.2.1 Impedance analysis of defective plates and ISP

The raw impedance spectra exhibited impulsive spikes due to electromagnetic noise and acquisition artifacts. The data were processed using a two-stage filtering pipeline to extract the underlying impedance. Impulsive spikes were removed using an outlier-rejection filter applied to Z(f). A Savitzky–Golay low-pass smoothing filter was used to recover the smooth impedance trend while preserving the frequency dependent curvature. The filtered $|Z|$–frequency curves presented in Figure 6 are the result of this procedure, whereas the Supplementary Material includes the raw data.

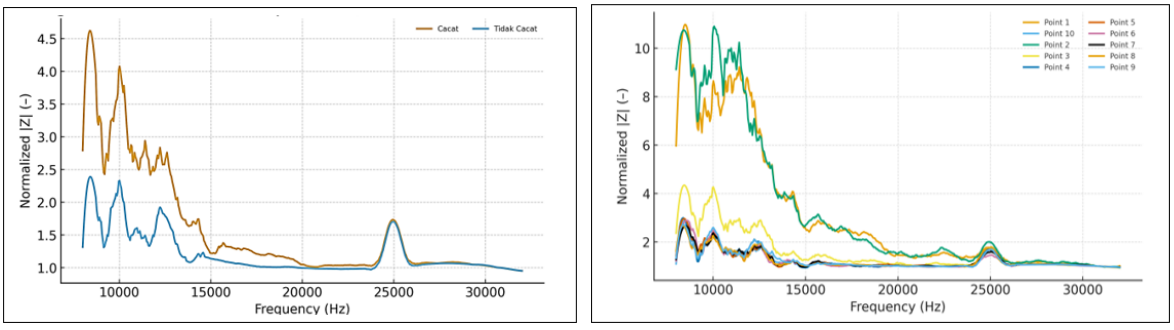

(a) (b)

Figure 6 Impedance values at 8 Hz–32 kHz on plate and pipe steel (a). Plate steel (b). Pipe steel

3.2.2 PCA base weld defect clustering

PCA was applied to the induced-voltage spectral features acquired by the CMI sensor over 8 Hz–32 kHz to separate the defective from the non-defective responses (Figure 7 and Figure 8).

- Two-dimensional PCA of a steel plate specimen

In Figure 7a, the nondefective samples form a tight cluster near the origin, whereas the defective samples primarily spread along PC1, indicating strong defect sensitivity. Separation in PC1–PC3 is weaker than that in PC1–PC2, that PC3 captures secondary variance; PC2–PC3 alone are insufficient, underscoring the dominant discriminative role of PC1.

- Two-dimensional PCA of a steel pipe specimen

For the industrial pipe (10 circumferential weld locations), Figure 7b. shows two clusters: points 1–4 (tight, near-origin; non-defective) and points 5–10 (more dispersed, mainly along PC1), consistent with PC1 carrying the dominant defect-related variance (skin-depth/eddy-current effects).

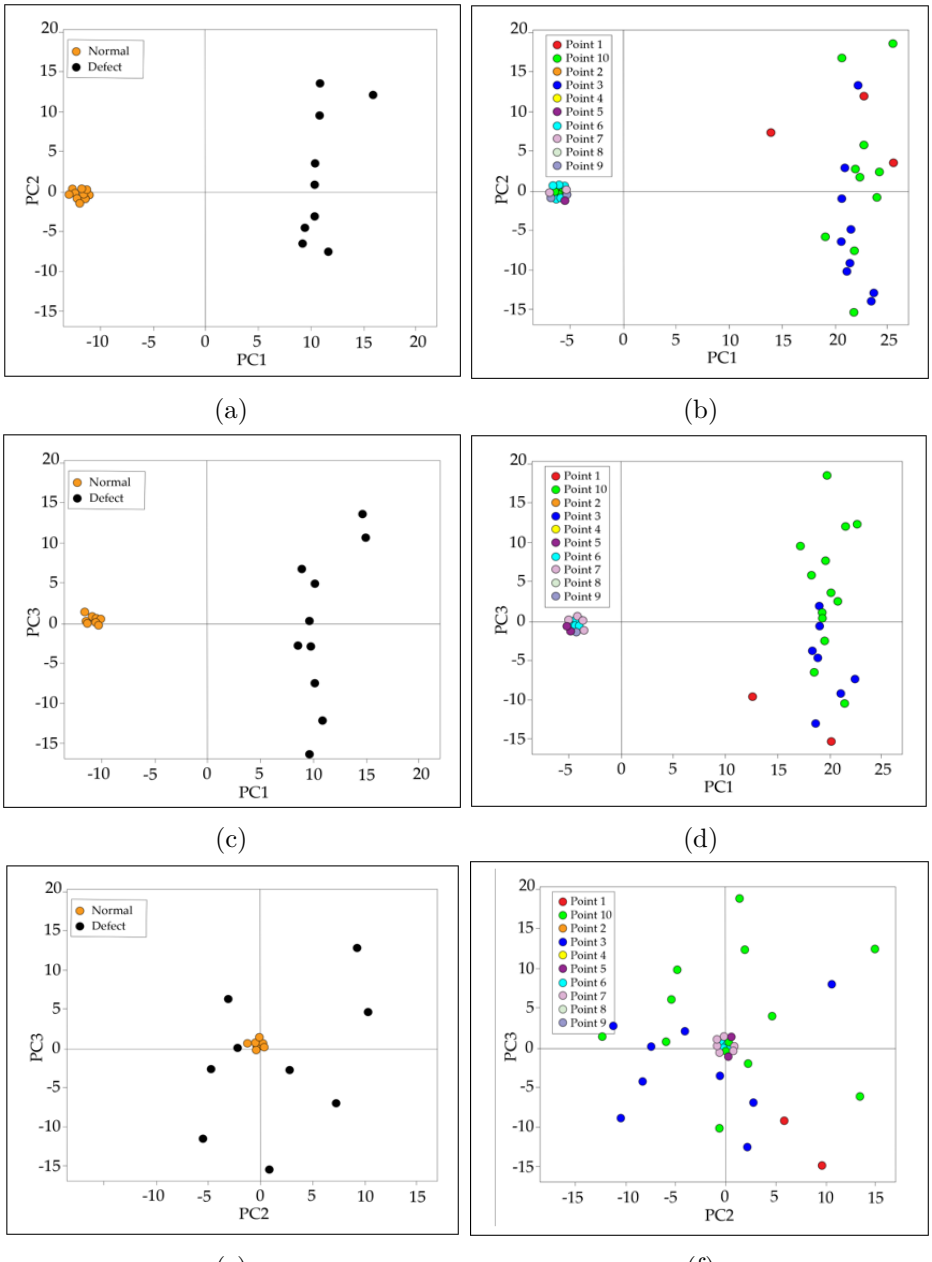

Figure 7 Two-dimensional PCA of the (a) PC1 vs. PC2 Plate (b) PC1 vs. PC2 Pipe (c) PC1 vs. PC3 Plate (d) PC1 vs. PC3 Pipe (e) PC2 vs. PC3 Plate (f) PC2 vs. PC3 Pipe

- Three-dimensional PCA (Plate and Pipe)

The combined 3D PCA (Figure 8) preserved the class separation for both specimens, with PC1 remaining the principal contributor to the between-class variance. This corroborates the 2D findings and supports the use of CMI-based spectral features to identify signal-level defects.

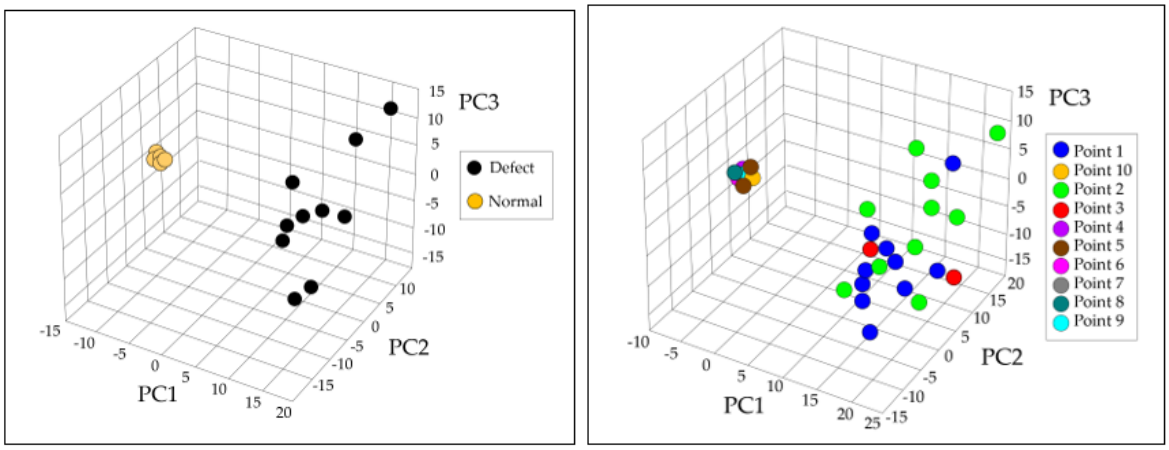

(a) (b)

Figure 8 Three-dimensional PCA at 8000–32000 Hz (a). Plate steel (b) Pipe steel

3.3 Validation of experimental data

Independent validation on the 40–100 kHz operating band demonstrated excellent repeatability (CV < 2.5%) and significant class differences (t-tests, all $p < 0.01$). PCA feature separability was further confirmed by Hotelling's T^2 ($p < 0.01$). The difference in bands (PCA at 8 - 32 kHz vs. statistics at 40–100 kHz) reflects complementary objectives: PCA captures the global low-band structure, whereas the 40–100 kHz band maximizes the measurement contrast for quantitative testing. Independent samples t-tests showed higher induced voltages for defective than non-defective specimens across the optimal band (all $p<0.01$), consistent with eddy-current and secondary-field perturbations. PCA features exhibited clear class separation by Hotelling's T^2 ($p<0.01$).

4. Conclusions

A CMI sensor was designed and validated for inspection of the steel pipe using multiphysics simulations and controlled experiments. The coaxial Tx–Rx geometry increased the electromagnetic coupling and sensitivity, and the optimal operating band of 40–100 kHz was identified to balance the skin depth and attenuation. On SS400 specimens with 0.5–2.0 mm artificial flaws, induced-voltage/impedance responses scaled with defect size; the 0.5 mm flaw remained above the noise floor, measurement variability was low (CV<2.5%), and group differences were statistically significant (t-test, $p < 0.01$). PCA achieved clear separation between defective and non-defective classes, corroborated by Hotelling's T^2 ($p < 0.01$). Collectively, these results indicated that the CMI sensor enables reliable sub-millimeter defect detection while offering a portable, radiation-free, and cost-effective alternative to RT. The remaining gaps, including detectability below 0.5 mm, calibration stability, and throughput, can motivate future work on coil optimization, automated scanning, multi-frequency excitation, ML-based classification, and large-scale field trials benchmarked against RT.

Acknowledgements

The authors would like to thank C-Tech Labs Edwar Technology, the Advanced Materials and Tomography Laboratory, Faculty of Engineering, Universitas Sultan Ageng Tirtayasa, and

the Faculty of Engineering, Universitas Indonesia, for their invaluable technical support and collaboration in this research. Funding: No external funding was received.

Conflict of Interest

The authors declare no conflict of interest related to the research, authorship, or publication of this article. The development of the CMI sensor, including its patent filing status, did not influence the objectivity of the results or conclusions. No financial or personal relationships have inappropriately affected the work reported in this manuscript.

Supplementary Materials

Supplementary materials associated with this study, including raw measurement data, additional figures, extended simulation results, and supporting documentation of the experimental setup, are available upon request from the corresponding author. These supplementary files are provided to ensure transparency, reproducibility, and completeness of the research presented in this study.

Declaration of AI Use

The authors declare that artificial intelligence (AI) tools (OpenAI ChatGPT, version 2025) were used solely to improve the readability, grammar, and clarity of the manuscript. AI tools were not used to generate scientific content, perform data analysis, conduct experiments, interpret results, or draw conclusions. All research ideas, methodologies, analyses, results, and interpretations presented in this manuscript are the authors' own work and responsibility.

References

Al Huda, M., Haryono, D., Nugraha, H., Fitriani, A. N., & Taruno, W. P. (2020). Characterization of magnetic induction coil sensor for void detection in steel plate. *2020 International Conference on Smart Technology and Applications (ICoSTA)*. https://doi.org/10.1109/ICoSTA48221.2020.1570610828

Cao, Z., Ye, B., Cao, H., Zou, Y., Zhu, Z., & Xing, H. (2024). Biplane enhancement coil for magnetic induction tomography of cerebral hemorrhage. *Biosensors*, *14*(5), 217. https://doi.org/10.3390/bios14050217

Chen, J., Ke, L., Du, Q., Zu, W., & Ding, X. (2019). Sector sensor array technique for high conductivity materials imaging in magnetic induction tomography. *Biomedical Engineering Online*, *18*, 1–16. https://doi.org/10.1186/s12938-019-0734-2

Deepak, J. R., Raja, V. K. B., Srikanth, D., Surendran, H., & Nickolas, M. M. (2021). Non-destructive testing techniques for low carbon steel welded joints: A review and experimental study. *Materials Today: Proceedings*, *44*, 3732–3737. https://doi.org/10.1016/j.matpr.2020.11.578

Dingley, G., & Soleimani, M. (2021). Multi-frequency magnetic induction tomography system and algorithm for imaging metallic objects. *Sensors*, *21*(11), 3671. https://doi.org/10.3390/s21113671

Feldkamp, J. R. (2017). Inversion of an inductive loss convolution integral for conductivity imaging. *Progress in Electromagnetics Research B*, *74*, 93–107. https://doi.org/10.2528/PIERB17021413

Grand View Research. (2024, March). Steel pipes tubes market (2024 - 2030) [Accessed March 2024].

Griffiths, H. (2001). Magnetic induction tomography. *Measurement Science and Technology*, *12*(8), 1126. https://doi.org/10.1088/0957-0233/12/8/319

Guan, K., Zhou, Y., Wang, L., Chang, B., & Du, D. (2025). A self-configuring transformer segmentation method for welding radiographic defect detection in steel pipes. *Non-*

destructive Testing and Evaluation, 1–22. https://doi.org/10.1080/10589759.2025.2491739

Guilizzoni, R., Finch, G., & Harmon, S. (2019). Subsurface corrosion detection in industrial steel structures. *IEEE Magnetics Letters*, *10*, 1–5.

Gupta, M., Khan, M. A., Butola, R., & Singari, R. M. (2022). Advances in applications of non-destructive testing: A review. *Advances in Materials and Processing Technologies*, *8*(2), 2286–2307. https://doi.org/10.1080/2374068X.2021.1909332

Haryono, D., Suandana, I. M. R. F., Sholehah, A., Nugraha, K., & Fadlil. (2024). Sensor arus eddy koaksial (coaxial eddy current sensor) [Indonesian Intellectual Property Database]. https://pdki-indonesia.dgip.go.id/detail/e3b0c44298fc1c149afbf4c8996fb92427ae41e4649b934ca495991b7852b855

Hofmann, A., Klein, M., Rueter, D., & Sauer, A. (2022). A deep residual neural network for image reconstruction in biomedical 3d magnetic induction tomography. *Sensors*, *22*(20). https://doi.org/10.3390/s22207925

Ishak, N., Lee, C. K., & Muji, S. (2021). Simulation magnetic induction tomography for agarwood using comsol multiphysics. *International Journal of Engineering and Advanced Technology*, *10*, 67–71. https://doi.org/http://www.doi.org/10.35940/ijeat.C2174.0210321

Klein, M., Erni, D., & Rueter, D. (2020). Three-dimensional magnetic induction tomography: Improved performance for center regions inside low conductive and voluminous body. *Sensors*, *20*(5), 1306. https://doi.org/https://doi.org/10.3390/s21227725

Kou, S. (2003). *Welding metallurgy*. John Wiley & Sons.

Ma, L. (2014). *Magnetic induction tomography for non-destructive evaluation and process tomography* [Doctoral dissertation, University of Bath].

Ma, L., & Soleimani, M. (2017). Magnetic induction tomography methods and applications: A review. *Measurement Science and Technology*, *28*(7), 072001. https://doi.org/10.1088/1361-6501/aa7107

Ma, L., Spagnul, S., & Soleimani, M. (2017). Metal solidification imaging by magnetic induction tomography. *Scientific Reports*, *7*(1), 14502. https://doi.org/10.1038/s41598-017-15131-z

Mansor, M. s. B., Zakaria, Z., Balkhis, I., Rahim, R. A., & Sahib, M. F. A. (2015). Magnetic induction tomography: A brief review. *Jurnal Teknologi*, *73*(3), 91–95. https://doi.org/10.11113/jt.v73.4252

Muttakin, I., & Soleimani, M. (2020). Magnetic induction tomography spectroscopy for metallic materials characterization. *Materials*, *13*(11), 2639. https://doi.org/10.3390/ma13112639

Muttakin, I., Wondrak, T., & Soleimani, M. (2020). Magnetic induction tomography sensors for visualization of liquid metal flow shape. *IEEE Sensors Letters*, *4*(7), 1–4. https://doi.org/10.1109/LSENS.2020.3000292

Noorsaman, A., Amrializzia, D., Zulfikri, H., Revitasari, R., & Isambert, A. (2023). Machine learning algorithms for failure prediction model and operational reliability of onshore gas transmission pipelines. *International Journal of Technology*, *14*(3), 680–689. https://doi.org/10.14716/ijtech.v14i3.6287

Nugraha, K., Winarto, W., Haryono, D., Sholehah, A., & Nugraha, H. (2025). Material characterization using magnetic induction based measurement technique at low-frequency range. *Journal of Physics: Conference Series*, *2980*(1), 012033. https://doi.org/10.1088/1742-6596/2980/1/012033

Nugraha, K., Winarto, W., Haryono, D., Sholehah, A., Widada, W., Nugraha, H., Sediyatmo, M., Muttakin, I., & Ramadhan, R. (2026). Simulation of weld defect detection in steel pipes using magnetic induction tomography sensor modeling. *Proceedings of the International Conference on Smart and Advanced Manufacturing*. https://doi.org/10.1007/978-981-96-9740-3_17

Pipeline and Hazardous Materials Safety Administration. (2022). Pipeline incident 20 year trends. https://www.phmsa.dot.gov/data-and-statistics/pipeline/pipeline-incident-20-year-trends

Piscitelli, G., Su, Z., Udpa, L., & Tamburrino, A. (2023). Magnetic induction tomography via the monotonicity principle. *Journal of Physics: Conference Series*, *2444*(1), 012005. https://doi.org/10.1088/1742-6596/2444/1/012005

Puji, M. N., Prajitno, P., & Taruno, W. P. (2024). Design of volumetric magnetic induction tomography system using comsol simulation. *2024 International Conference on Radar, Antenna, Microwave, Electronics, and Telecommunications (ICRAMET)*. https://doi.org/10.1109/ICRAMET62801.2024.10809219

Ratajczak, M., & Wondrak, T. (2020). Analysis, design and optimization of compact ultra-high sensitivity coreless induction coil sensors. *Measurement Science and Technology*, *31*(6), 065902. https://doi.org/10.1088/1361-6501/ab7166

Schledewitz, T., Hofmann, A., Fehr, M., Sauer, A., & Rueter, D. (2024). Hybrid method for image reconstruction in magnetic induction tomography: Combination of the neural network with an iterative analytical algorithm. *Current Directions in Biomedical Engineering*. https://doi.org/10.1515/cdbme-2024-2134

Schledewitz, T., Klein, M., & Rueter, D. (2023). Magnetic induction tomography: Separation of the ill-posed and non-linear inverse problem into a series of isolated and less demanding subproblems. *Sensors*, *23*(3). https://doi.org/10.3390/s23031059

Shaloo, M., Schnall, M., Klein, T., Huber, N., & Reitinger, B. (2022). A review of non-destructive testing (ndt) techniques for defect detection: Application to fusion welding and future wire arc additive manufacturing processes. *Materials*, *15*(10), 3697. https://doi.org/10.3390/ma15103697

Tan, C., Chen, Y., Wu, Y., Xiao, Z., & Dong, F. (2021). A modular magnetic induction tomography system for low-conductivity medium imaging. *IEEE Transactions on Instrumentation and Measurement*, *70*, 1–8. https://doi.org/10.1109/TIM.2021.3073439

Wei, H. Y., Ma, L., & Soleimani, M. (2012). Volumetric magnetic induction tomography. *Measurement Science and Technology*, *23*(5), 055401.

Wei, H. Y., & Soleimani, M. (2012). A magnetic induction tomography system for prospective industrial processing applications. *Chinese Journal of Chemical Engineering*, *20*(2), 406–410. https://doi.org/10.1016/S1004-9541(12)60404-2

Xiao, Z., Tan, C., & Dong, F. (2019). Three-dimensional hemorrhage imaging by cambered magnetic induction tomography. *IEEE Transactions on Instrumentation and Measurement*, *68*(7), 2460–2468. https://doi.org/10.1109/TIM.2019.2900779

Yang, D., Liu, J., Wang, Y., Xu, B., & Wang, X. (2021). Application of generative adversarial network in image reconstruction of magnetic induction tomography. *Sensors*, *21*(11), 3869. https://doi.org/10.3390/s21113869

Zhu, Z., Tan, C., Chen, Y., & Dong, F. (2023). Hemorrhage detection by magnetic induction tomography with helmholtz coil. *42nd Chinese Control Conference*. https://doi.org/10.23919/CCC58697.2023.10240606